Effect of dip-coating cycle on some physical properties of Cu$_2$NiSnS$_4$ thin films for photovoltaic applications

Ahmed Ziti[1,*] , Bouchaib Hartiti[1], Amine Belafhaili[4], Hicham Labrim[3], Salah Fadili[1], Abderraouf Ridah[2], Mounia Tahri[3], and Philippe Thevenin[5]

[1] ERDyS Laboratory, MEEM & DD Group, Hassan II University of Casablanca, FSTM, BP 146, 20650 Mohammedia, Morocco
[2] LIMAT Laboratory, Department of Physics FSB, Hassan II University of Casablanca, Casablanca, Morocco
[3] DERS, CNESTEN, Rabat, Morocco
[4] Centre for Electron Microscopy, Faculty of Sciences, Mohammed V University, Rabat, Morocco
[5] University of Lorraine, LMOPS, METZ, Metz, France

ABSTRACT

Quaternary semiconductor Cu$_2$NiSnS$_4$ thin film was made by the sol–gel method associated with dip-coating technique on ordinary glass substrates. In this paper, we have studied the impact of dip-coating cycle at different cycles: 4, 5 and 6 on the structural, compositional, morphological, optical and electrical characteristics. CNTS thin films have been analyzed by various characterization techniques including X-ray diffractometer (XRD), Raman measurements, scanning electron microscope (SEM), energy-dispersive X-ray spectroscope (EDS), UV–Visible spectroscopy and four-point probe method. XRD spectra demonstrated the formation of cubic Cu$_2$NiSnS$_4$ with privileged orientation at (111) plane. Crystallite size of cubic CNTS thin films increases from 6 to 9 with augmentation of dip-coating cycle. Raman scattering confirmed the existence of CNTS thin films by Raman vibrational mode positioned at 332 cm^{-1}. EDS investigations showed near-stoichiometry of CNTS sample deposited at five cycles. Scanning electron microscope showed uniform surface morphologies without any crack. UV–Vis spectroscopy indicated that the optical absorption coefficient values are larger than 10^4 cm^{-1}. Estimated band gap energy of CNTS absorber layers decreases from 1.64 to 1.5 eV as dip-coating cycle increased. The electrical conductivity of CNTS thin films increases from 0.19 to 4.16 $(\Omega\,\text{cm})^{-1}$. These characteristics are suitable for solar cells applications.

Address correspondence to E-mail: ziti.ahmed91@gmail.com

1 Introduction

The costly and scarcity of galium (Ga) and indium (In) and toxicity of cadmium (Cd) limited the future of high-efficient copper indium gallium sulfur CuInGaS$_2$ and cadmium telluride CdTe absorbers materials [1, 2]. Due to these problems, the quaternary semiconductor Cu$_2$ZnSnS$_4$ (CZTS) is emerged as interest and appropriate absorber layer in photovoltaic solar cell-based thin films during several years; CZTS thin film is low cost and abundant in earth crust [3–5]. The power conversion efficiency of 12.6%, but this efficiency does not improved from 2014 until this year [6]. In addition, Cu$_2$ZnSnS$_4$ has a wider range of possible defects depending on its growing conditions and variations in stoichiometry, most of the anti-sites Cu$_{Zn}$, Sn$_{Zn}$, and Zn$_{Sn}$) [7], and these defects influence negatively the efficiency of CZTS solar cells. Apparently, the studies of semiconductors absorbers can be classified in two major axes: The improvement of CZTS thin film in solar cell for photovoltaic application [8], and the amelioration of solar cell performances using a novel approach, has entice serious intension in 2020 from some research investigations is the substitution Zn^{2+} by other elements has similar valence electronic including Mn^{2+}, Mg^{2+}, Fe^{2+}, Co^{2+}, Ba^{2+}, Ni^{2+}. These research lead to develop the novel low-cost semiconductors absorbers layers Cu$_2$MnSnS$_4$, Cu$_2$MgSnS$_4$, Cu$_2$FeSnS$_4$, Cu$_2$CoSnS$_4$, Cu$_2$BaSnS$_4$ and Cu$_2$NiSnS$_4$ [9–14]. These quaternaries can be used in various applications such as photolysis, sensors, thermoelectricity, batteries, spintronics and photovoltaics. Copper nickel tin sulfur Cu$_2$NiSnS$_4$ (CNTS) is presently adaptable compound for photovoltaic solar cells, thanks to its high optical absorption coefficient α (superior to 10^4 cm^{-1}), band gap range of 1.2–1.7 eV and p-type semiconductor material [15–17]. In addition, CNTS does not contain scarce and cost chemical elements like indium (In) and gallium (Ga), and the elements constituents of CNTS are economical and abundant in earth-crust. The high conversion efficiency of CNTS solar cell absorber layer is 8.2% achieved by Lu et al. [18]; this efficiency is near to high efficiency of CZTS absorber material and motivates the effort in CNTS compound. Various methods are applied for synthesis of CNTS thin films such as spray pyrolysis [19], electrodeposition [20], solvothermal [21], hydrothermal [22], hot injection [23], spin coating [24], dip-coating [25]. Dip-coating method is suitable for the preparation of homogenous CNTS thin films because it leads to deposit the sol–gel solution over large areas by ensuring the control of film thickness and film structure using the dip-coating speed and dip-coating cycle [26]. In general, dip-coating technique is commonly used due to its versatility in elaboration thin films with appropriate homogeneity on all types of substrates [27]. Also this technique is less used for the preparation of CNTS semiconductor compound material. The annealing in air is simple, environmental friendly compared to annealing under other toxic gases such as H$_2$S and argon.

Some groups have studied CNTS thin layers by different preparation methods, and Chen et al. elaborate uniform Cu$_2$NiSnS$_4$ thin layer by electrochemical deposition method and obtain a cubic zinc blend structure, great absorption coefficient and optical energy gap approximated to be 1.2 eV [28]. Yang et al. synthesized CNTS absorber materials using a single step electrodeposition method and found pure stannite structure and optical energy gap around 1.61 eV [27]. Ghosh et al. fabricated solar cell based on CNTS absorber layer ITO/ZnO–NR'S/ZnS/Cu$_2$NiSnS$_4$/Au under AM1.5 standard light condition and achieved the conversion efficiency of 2.71% with band gap of 1.74 eV, with the solar cell parameters such as: V_{oc} = 0.77 V, FF = 0.537 and J_{sc} = 7.83 mA/cm^2 [29]. Rondiya et al. elaborated cubic zinc blend CNTS thin layers, the approximated optical band gap energy around 1.57 eV and absorption coefficient over to 10^5 cm^{-1}. The realized solar cell glass/Mo/CNTS/CdS/Al-ZnO/Al reported the efficiency (η) of 0.09%, V_{oc} equal to 423.80 mV, J_{sc} equal to 0.52 mA/cm^2 and FF equal to 0.43 [30].

In our work, we investigated the preparation of CNTS thin films by sol–gel method, associated with simple and economical dip-coating technique, on the ordinary glass substrates without sulfurization process. We focused on the effect of dip-coating cycle: 4, 5 and 6 using a speed of 50 mm/min on the some physical properties such as structural, compositional, morphological, optical and electrical properties. We also, calculated some optical parameters including refractive index, extinction coefficient, imaginary and real dielectric constants and optical conductivity to improve the optical devices.

2 Experimental detail

CNTS thin layers were synthesized by sol–gel approach, in which the initial solution is elaborated from copper chloride $CuCl_2$ (II), nickel chloride $NiCl_2$ (II), tin chloride $SnCl_4$ (IV) and thiourea $SC(NH_2)_2$. These precursors were utilized as bases of diverse chemical elements (Cu, Ni, Sn and S) in the ratio of: $\frac{Ni}{Sn} = 1.1$, $\frac{Cu}{Ni+Sn} = 0.85$ and $\frac{S}{Cu+Ni+Sn} = 1.9$. These salts are dissolved in isopropyl alcohol (30%) and distilled water (70%), and the solution was agitated magnetically during 30 min at 50 °C. A clear and homogenous green solution was prepared directly after addition of thiourea. The ordinary glass substrates were cleaned with distilled water, diluted nitric acid and isopropyl alcohol. The sol–gel CNTS solution was dip-coated at a speed of 50 mm/min on the ordinary glass substrates at a different dip-coating cycle: 4, 5 and 6. The CNTS samples were annealed at 300 °C for 5 min in air. The thicknesses of CNTS thin films are estimated in the range of 1.60–1.71 μm. The dip-coated CNTS samples were characterized using X-ray diffractometer (XRD), with CuKα radiation (λ = 1.54056 Å) in angle 2θ range of 20°–65° (D2 Phaser-Bruker), and Raman spectroscopy, using a laser excitation wavelength λ = 532 nm in the Raman shift from 100 to1000 cm^{-1} to study structural properties. The compositional and morphological properties were controlled using an energy-dispersive X-ray spectroscopy (EDS) and scanning electron microscopy (SEM) [Jeol scanning microscopy IT 100 (JSM-IT 100)]. The optical characteristics were studied by using UV–Visible spectrophotometer in the wavelength range of 475–850 nm (Spectrovio junior kit-SV2100). The electrical properties were measured using the four-point probe method for calculating the resistivity conductivity of CNTS thin films.

3 Results and discussion

3.1 Structural properties

Figure 1 presents the X-ray diffraction patterns of CNTS thin films elaborated at different dip-coating cycles. Broad peaks are located at 2θ around 28.45°, 32.56° and 47.48° matching, respectively, to (111), (200) and (220) planes, the high intensity of peak
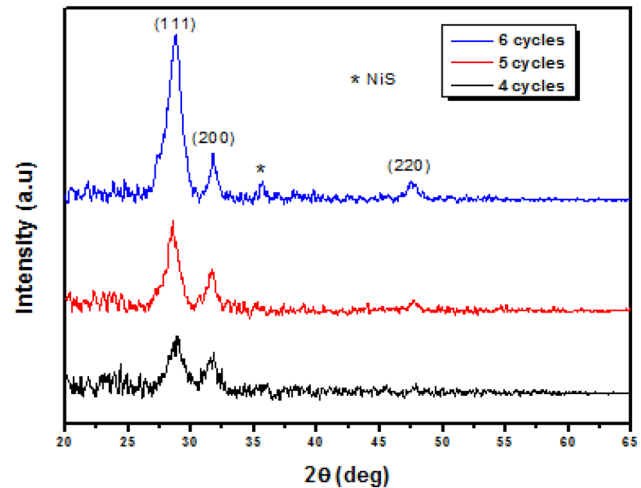
Fig. 1 X-ray diffraction peaks of CNTS thin films dip-coated at various cycles

located at 28.45° showed privileged direction along (111) plane, the preferentially direction of (111) plane and peaks proved the formation of cubic CNTS phase corresponding to (JCPDS card No. 00-026-0552). These results are similar to those reported using different research groups [14]. No other additional phases are presented in the films deposited at four cycles and five cycles, and we have shown the formation of NiS secondary phase in the film deposited at six cycles. The formation of these phases is probably due to high quantity of nickel (Ni) in sample dip-coated at six cycles, and the high adhesion of Ni compared to Sn for this film leads to the Ni-S formation due to high electronegativity of sulfur. The intensity of (111) plane increased when dip-coating cycle increased; this indicates the amelioration of the CNTS quality with increasing of dip-coating cycle. The crystallinity of the CNTS thin films is ameliorated in the adhesion of layer by layer when dip-coating cycle equals 6. The sharp and intense (111) peak of the sample dip-coated at six cycles shows an appropriate crystallinity of the CNTS thin film.

Crystallite size (D) of CNTS thin layers was approximated from Scherrer's relation (1):

$$D = \frac{0.94\lambda}{\beta \cos(\theta)} \qquad (1)$$

where λ is the wavelength of the X-ray diffract-meter (λ = 1.54056 Å), β is the full-width at half maximum (FWHM), θ is an angle of the Bragg diffraction. The estimated crystallites size of deposited CNTS thin films with different dip-coating cycle is summarized

in Table 1. The crystallites size has increased from 6 to 9 nm with the increase of dip-coating cycle. High quantity of CNTS solution was adsorbed in the substrate. In the annealing process, compact materiel quantity indicates easy germination of grain and condensation of CNTS thin films, which leads to the formation of higher crystallite size. This behavior proves the high crystallinity and low defects like dislocations density and microstrain in a dip-coated CNTS semiconductor material. Those results prove indeed that increasing the cycles of dip-coating leads to the enhancement of thin films quality.

Dislocation density (ρ) shows the defects quantity of dip-coater CNTS thin layer structure. "ρ" is distinct as the dislocation length lines per unit volume of the elaborated CNTS semiconductor compound material [31]. In general, great crystallite size of compound thin layers indicates smaller dislocation density [31]. The microstrain (ε) is linked to some annealing and deposition conditions, and the approximated number of crystallite is calculated using film thickness (e) and crystallite size (D) of CNTS thin films. To investigate certain structural parameters along (111) plane of CNTS films, dislocation density, microstrain and crystallite number were approximated following the equations:

$$\varepsilon = \frac{\beta \ \cos(\theta)}{4} \tag{2}$$

$$\rho = \frac{1}{D^2} \tag{3}$$

$$N = \frac{e}{D^3} \tag{4}$$

To control the vibrations modes and to confirm the phase identification of cubic Cu_2NiSnS_4 Raman measurements was used for analyzing various samples, we notice from Fig. 2 one Raman peak at 332 cm^{-1} shown for the samples dip-coated at 4 and 6 cycles. It is identified for cubic CNTS structure agreeing to results reported in the literatures [32]. No
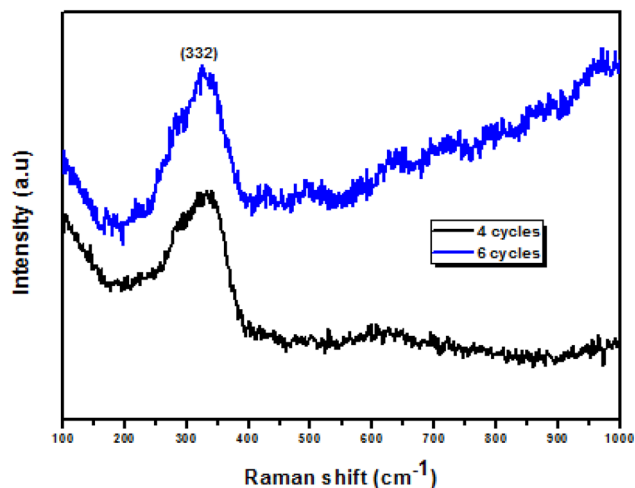
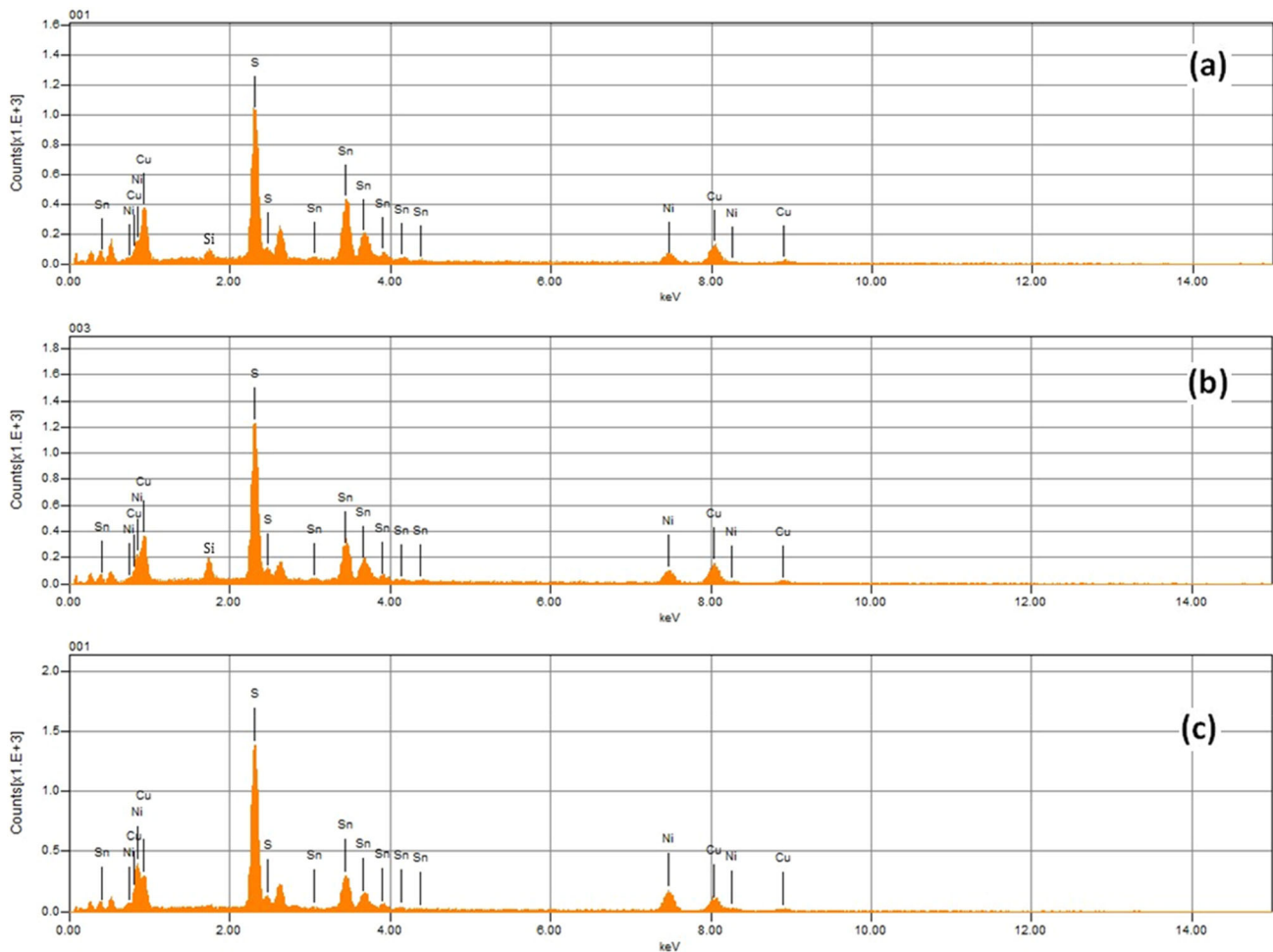**Fig. 2** Raman scattering measurements of CNTS deposited at four and six cycles

other ternary and binary secondary phases such as SnS_2 (Raman peaks at: 205 and 312 cm^{-1}) [33], SnS (Raman peaks at: 94, 160, 185 and 214 cm^{-1}) [31], Cu_2S (Raman peaks at: 410, 267 and 475 cm^{-1}) [34] and NiS (Raman peaks: 143, 240, 299, 345 and 371 cm^{-1}) [35] exist with CNTS phase. The NiS secondary phase in XRD patterns is not obtained in Raman spectrum of the sample dip-coated at six cycles which indicate the lower quantity of this phase compared to CNTS phase.

3.2 Compositional and morphological properties

Energy-dispersive X-ray spectroscopy (EDS) was utilized to control the atomic percentages of four constitutions elements (Cu, Ni, Sn and S) in CNTS layers with various dip-coating cycles. The EDS spectra of CNTS thin films are shown in Fig. 3. We indicate in Table 2 the presence of different chemical composition elements of CNTS thin films. The percentage of Cu is obtained in the range of 17.27–21.15%, and the percentage of Ni increased

Table 1 Structural information of Cu_2NiSnS_4 thin films at (111) plane

Dip-coating cycle	Crystallite size D (nm)	Dislocation density (ρ) $\times 10^{16}$ (Lines/m^2)	Microstrain (ε) $\times 10^{-2}$	Crystallite number (N) $\times 10^{18}$ (m^{-2})
4	6	2.51	2.34	6.39
5	8	1.41	1.76	2.80
6	9	1.10	1.55	1.98

Fig. 3 EDS spectra of CNTS thin films deposited at **a** four cycles, **b** five cycles and **c** six cycles

Table 2 EDS analysis of CNTS thin films

Dip-coating cycle	Cu	Ni	Sn	S	Ni/Sn	Cu/(Ni + Sn)	S/(Cu + Ni + Sn)
4	20.66	8.79	21.64	48.91	0.40	0.67	0.95
5	21.15	12.47	15.13	51.13	0.82	0.76	1.04
6	17.27	16.25	14.13	52.35	1.15	0.56	1.09

with increasing of dip-coating cycle from 8.79 to 16.25%. We can say from this results that nickel(Ni) is more adhesive with increasing of dip-coater cycles, and this behavior confirms the existence of NiS secondary phase in CNTS thin layer deposited at six cycles. Because in CNTS thin film is dip-coated at four cycles, the low quantity of nickel and sulfur indicates the defects vacancies in these elements of the film which leads to deviate the stoichiometry. In the sample deposited at five cycles, we obtain the near ideal percentage of Cu, Ni, Sn and S elements indicating close stoichiometric CNTS thin film. When

dip-coating cycles reached to 6, we have observed the saturation of material by 16.25% for Ni and 52.35% for S elements. With high quantity of these elements compared to ideal percentage, nickel and sulfur can be allied; this leads to deviate the stoichiometry and shows the formation NiS secondary phase. Also the percentage of Sn decreased, with increasing of dip-coating cycle, from 21.64 to 14.13%, the quantity of sulfur has increased slightly from 48.91 to 52.35%. These percentage close to ideal percentage 50%, despite of annealing without the use of sulfurization approach in toxic gases like H_2S and argon. From the

atomic percentages of four chemical elements and the ratios of Ni/Sn, Cu/(Ni + Sn) and S/(Cu + Ni + Sn), we have shown that CNTS sample dip-coated at five cycles is near to stoichiometry. The obtained results have motivated the research about CNTS thin layers for photovoltaic solar cells.

Figure 4 presents the scanning electronic microscope images of CNTS thin films dip-coated at various cycles. We see from Fig. 4 that all films indicated high-quality SEM images uniform without any crack. This images are suitable for photovoltaic applications. The film deposited at four cycles presented granular surface morphology, the film deposited at five cycles indicates the increasing of grain size and high grain size is observed in the film dip-coated at six cycles; also the density of films increased with increased dip-coating cycles. The latter is due to more adsorption of CNTS material with a deposition of six cycles. The uniformity of films indicates the high distribution of copper–nickel–tin–sulfur on the all surface of films and proved the EDS results.

3.3 Optical properties

We can evaluate transmittance (T) and absorbance (Abs) spectra from spectrophotometer UV–Vis to investigate the absorbance and transparency of films. Figure 5 shows measured optical transmittance as
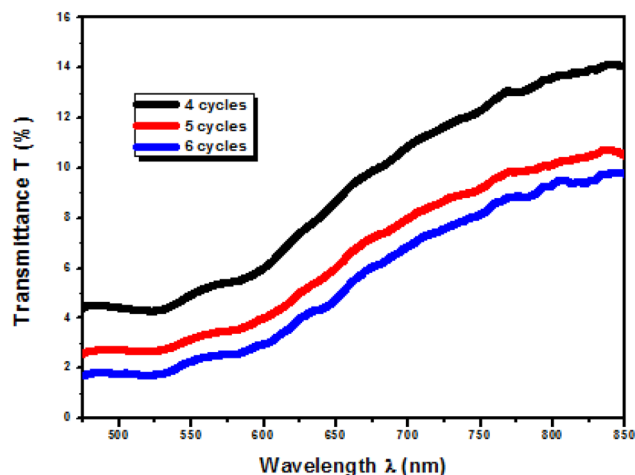
Fig. 5 Transmittance data as a function wavelength λ of CNTS absorber layers

function of wavelength λ in the range of 475–850 nm, and we can observe from this figure that transmittance of thin films decreases with increased dip-coating cycle, and the maximum transmittances of CNTS thin films deposited at four, five and six cycles are 14.14%, 10.84% and 9.83%, respectively. This behavior is due to the more absorption of incident photon energy from CNTS thin films with increased dip-coating cycles, also due to increasing of films thickness with increasing of adsorption layers. In addition, the decreasing of transmittance spectra with
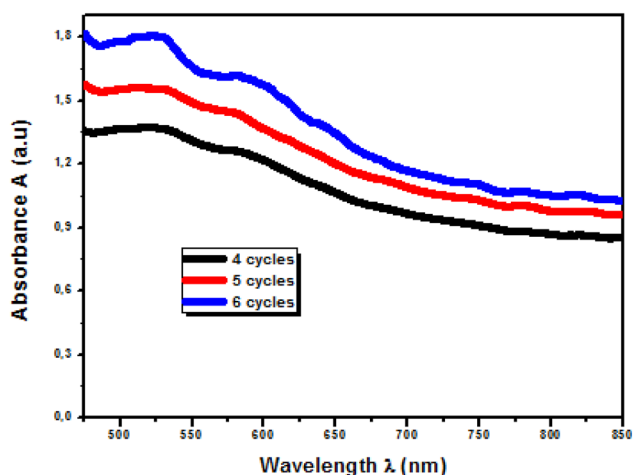

Fig. 4 SEM images of Cu_2NiSnS_4 thin films dip-coated at **a** four cycles, **b** five cycles and **c** six cycles
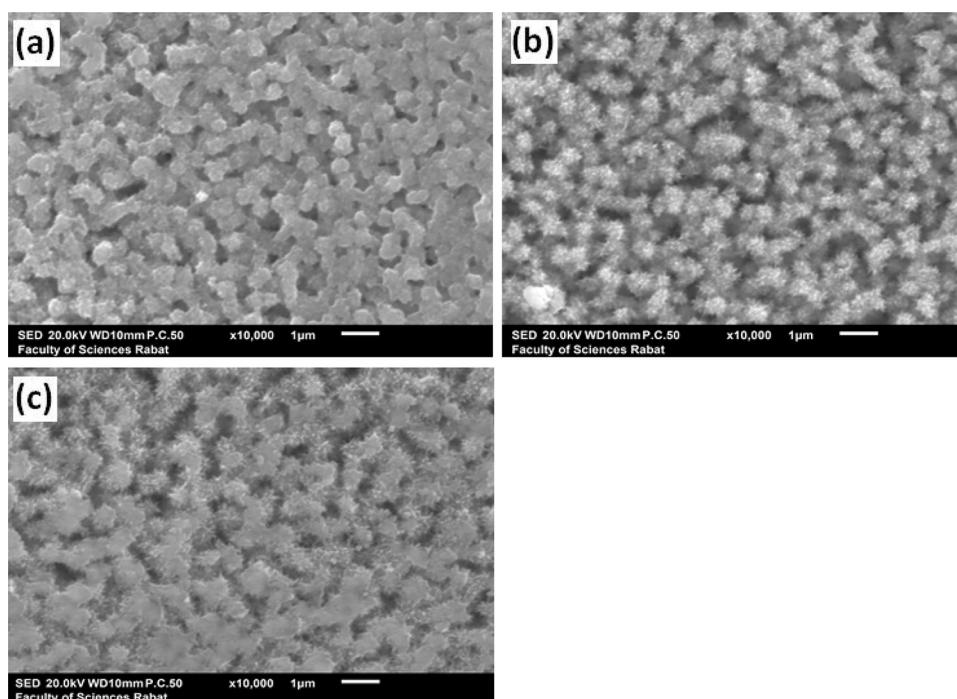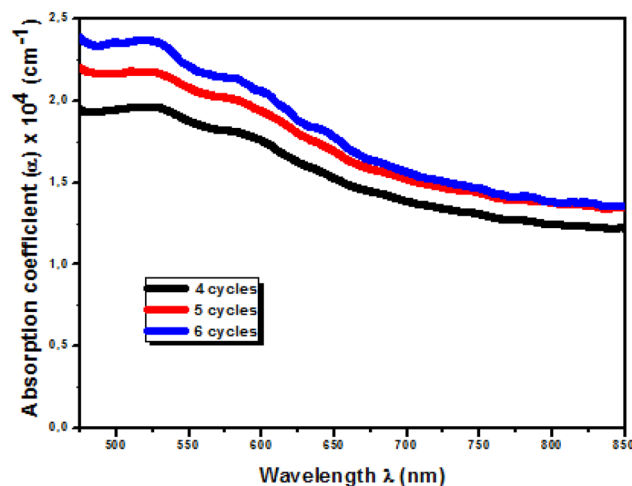
increasing of annealing temperature confirms the increasing of film densities. The low transmittances demonstrate that CNTS is suitable as absorber material in the solar cell-based thin layers. Figure 6 indicates the variation of optical absorbance versus wavelength λ. The optical absorbance spectra increased with increased annealing temperature, and the values of measured optical absorbance in the wavelength 475 nm are 1.34, 1.56 and 1.80 for the CNTS films deposited at four, five and six cycles, respectively. These values motivate the future research on CNTS thin films as alternative absorbers materials for solar cells applications. These results are comparable to the reported Ramírez et al. for sprayed Cu_2ZnSnS_4 [36]. Also, with those obtained by Ghediya et al. for CCTS absorber materials deposited by dip-coating technique [37] and Elsaeedy for CNTS absorber layers deposited by spray pyrolysis method [14].

Optical absorption coefficient (α) of Cu_2NiSnS_4 thin layers is calculated from film thickness and optical absorbance data using relation (5) [38]. Figure 7 presents the variation of absorption coefficient values as a function of wavelength λ, the absorption coefficient increased with dip-coating cycle, and these values are in the range of $1.20–2.38 \times 10^4$ cm^{-1}. The values of "α" are comparable to other research works on thin films absorber layers [19, 38, 39], and these values are adaptable to photovoltaic conversion solar energy.

$$\alpha = \frac{1}{e} \ln\left(\frac{100}{T}\right) \tag{5}$$

Fig. 7 Absorption coefficient of CNTS absorber materials

The optical energy gap is an essential in optical devices, and the band gap of thin film absorber layer is considered the lower compared to buffer and window thin films in solar cell; the band gap of window layer is considered the higher for maximize the transmittance of photon energy from this layer. The band gap of buffer layer is higher than the band gap of absorber layer and lower than the band gap of window layer; the role of this layer is to avoid electron hole recombination, so to found adaptable absorber material it is necessary to obtain the band gap range of 1.4–1.7 eV [40, 41]. The band gap of CNTS layers is estimated from Tauc's relation (6):

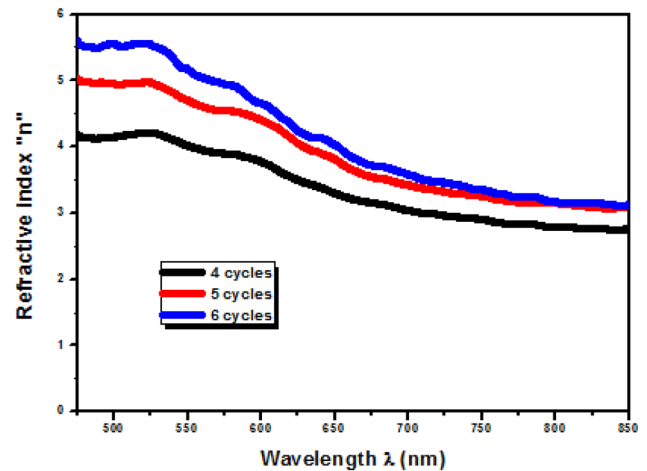$$(\alpha h \nu) = A(h\nu - E_g)^m \tag{6}$$

where A is proportionality constant; h is constant of Planck's, m is signifies the transition nature, m can take up a $\frac{1}{2}$ for direct allowed change and 2 for an indirect allowed change, 3 for indirect forbidden change, and $\frac{3}{2}$ for direct forbidden change. The CNTS absorber semiconductor has a direct allowed variation. The optimum band gap of quaternary absorber layers is 1.5 eV. The optical energy gap was estimated by extrapolating the lined part of $(\alpha h \nu)^2$ vs hν to (αhν) = 0 shown in Fig. 8. The band gap energies are 1.64, 1.56 and 1.5 eV for CNTS samples dip-coater at four, five and six cycles, and the band gap decreased with increasing of dip-coating cycle. This behavior is probably due to increasing of film thickness and increase in density of CNTS thin films with dip-coating increased. The NiS secondary phase does not affect negatively the band gap. These results are similar to the archived by Bakr et al. of CZTS thin

Fig. 6 Absorbance spectra as a function of wavelength λ of CCNTS absorber layers
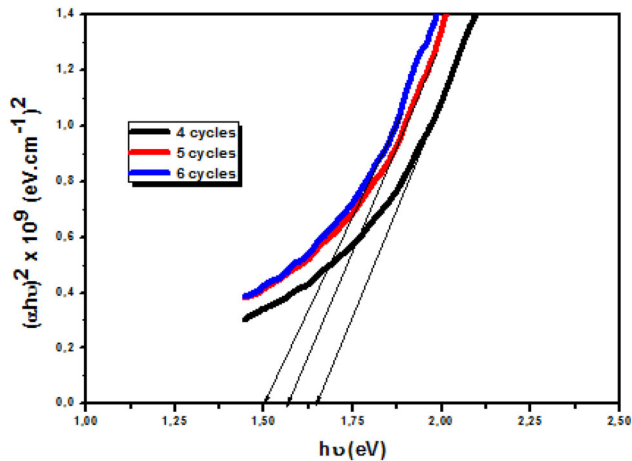
Fig. 8 Approximation of band gap by extrapolation method from the variation of $(\alpha h\nu)^2$ as a function of hν for Cu_2NiSnS_4 thin films

Fig. 9 Refractive index versus wavelength λ of CNTS thin films

films synthesis by chemical spray pyrolysis [42], also Maldara et al. for CCTS thin films prepared by spray pyrolysis method [40], and Abed et al. for sprayed CNTS absorber materials [43]. The band gap of 1.5 eV showed CNTS thin film dip-coated at six cycles is the theoretical optimum value of semiconductors absorber thin films of solar cells realization [44].

The investigation of optical parameters such as refractive index (*n*), extinction coefficient (*k*), Real (ε_r) and imaginary (ε_i) dielectric constants and optical conductivity (σ_{opt}) is interesting for the amelioration and enhancement of solar cells devices. Refractive index is the more critical optical parameter of semiconductor thin films, because of it is linked to electronic polarization and interior local field semiconductor material. The values of refractive index was calculated using relation (7) by utilization of reflectance values and extinction coefficient values. The values of reflectance are calculated from measured absorbance and transmittance data (relation (8)) [45]. Figure 9 shows the optical refractive index as a function of wavelength λ; from this figure and Table 3, we show that refractive index has increased with increased annealing temperature. The greater values of "*n*" of the dip-coater CNTS thin films in function of dip-coating cycles can be clarified by the densification of our layers. When dip-coating cycle increased, the surface morphology is more and more dense and this causes a decrease in the light speed through the CNTS absorber layer and this leads to increase the values of "*n*." This result is in good agreement with SEM images of CNTS thin films,
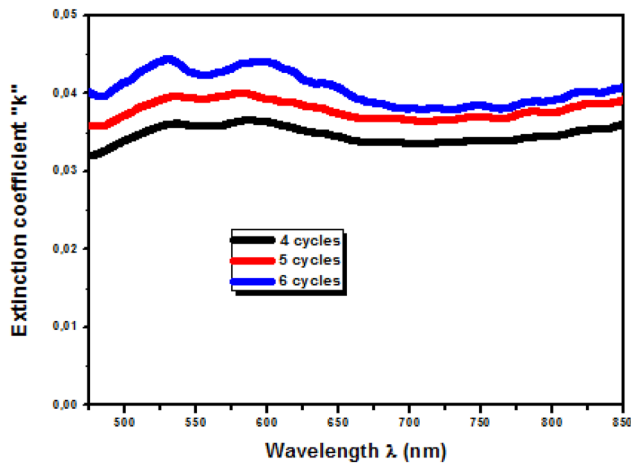
which present densely packed surface morphology for high dip-coating cycle. It can be, consequently, concluded that a thin layer with an important density presents the strong refractive index values given in Fig. 4. The refractive index values decrease versus wavelength λ which indicates normal dispersion behavior. The values of refractive index are in the range of 2.71–5.69 in the wavelength from 475 to 850 nm, and these values are appropriate for CNTS compound for solar cells applications. Also they are compared to those reported by other research studies for absorber materials [46, 47].

The extinction coefficient (*k*) shows the total optical waste brought around by scattering and optical transmittance of incident light. Similarly, the parameter "*k*" signifies the absorption quantity of photon energy in the thin layer semiconductor material, which means the extenuation of an electromagnetic wavelength that is traveling in a thin film material, and the values of optical extinction coefficient were calculated from wavelength λ and absorption coefficient using relation (9). Figure 10 presents the optical extinction coefficient as a function of wavelength λ. From Fig. 10 and Table 3, we indicate that extinction coefficient increased while increasing dip-coating cycle; this behavior is attributed to the increasing of "α" values with increasing of dip-coating cycle. In addition, this is probably attributed to similar reason specified earlier in the refractive behavior, and the values of extinction coefficient are in the range of 0.033–0.044. These small values are due to strong optical absorbance of all CNTS absorber material, and these values are

Table 3 Values of some optical parameters of Cu_2NiSnS_4 absorber materials in the wavelength λ 800 nm

Dip-coating cycle	Absorption coefficient $(\alpha) \times 10^4$ cm^{-1}	Refractive index (n)	Extinction coefficient (k)	Real dielectric constant (ε_r)	Imaginary dielectric constant (ε_i)
4	1.24	2.77	0.034	7.78	0.19
5	1.36	3.10	0.037	9.76	0.23
6	1.38	3.19	0.039	10.20	0.25

Fig. 10 Optical extinction coefficient versus wavelength λ of Cu_2NiSnS_4 thin films

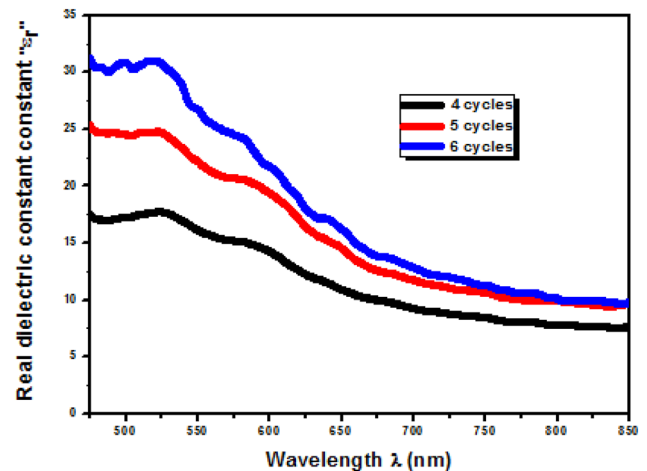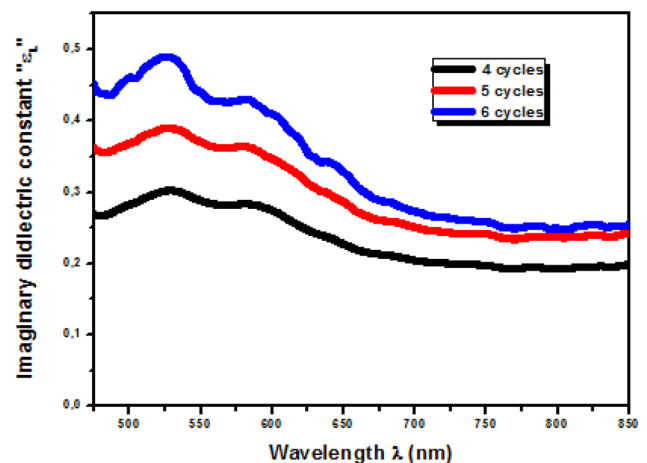**Fig. 11** Real dielectric constant of quaternary CNTS thin films

comparable to other groups for quaternary absorber layers [48, 49].

$$n = \frac{1+R}{1-R} + \sqrt{\frac{4R}{(1-R)^2} - k^2} \qquad (7)$$

$$R = \left[1 - \left(\frac{T}{\exp(-A)}\right)\right]^{1/2} \qquad (8)$$

$$k = \frac{\alpha\lambda}{4\pi} \qquad (9)$$

The optical dielectric constant is an intrinsic optical parameter to express the optical behavior of a thin layer semiconductor material. This parameter can be valued using the values of "n" and the values of "k" (relations 10 and 11). The complex dielectric constant equation is expressed using $\varepsilon = \varepsilon_r + i\varepsilon_i$ where "ε_r" and "ε_i" are real and imaginary dielectric constants, respectively. "ε_r" is joined to the deceleration of the light speed and "ε_i" is related to the interaction of electric field with a matter. The values of dielectric constants were calculated using equations below and are exhibited in Figs. 11 and 12.

Fig. 12 Imaginary dielectric constant of deposited CNTS thin films

$$\varepsilon_r = n^2 - k^2 \qquad (10)$$

$$\varepsilon_i = 2nk \qquad (11)$$

From Fig. 11 and Table 3, we can show that the real dielectric constant has increased with dip-coating cycle increased, in the wavelength λ range of 475–850 nm. This behavior is attributed to the strong

dispersion caused by the increase of dip-coating cycle. The real dielectric constant values are determined from 7.56 to 31.41 in the wavelength range of 475–850 nm. According to relation (10), the values of real dielectric constant are depending usually on the values refractive index (n^2) because the values of extinction coefficient (k^2) are minor compared to n^2. Figure 12 shows the imaginary dielectric constant as a function of wavelength λ, the imaginary dielectric constant increases with dip-coating cycle increased. This behavior is due to the rise in the extinction coefficient values. The imaginary dielectric values are found ranging from 0.19 to 0.49. The superior value of "εi" is assigned to the losses made by the optical absorbance. The more optical absorbance can reason major losses inside the thin film material. These established results are in good agreement to other research works on absorber materials [39, 47]. The values of optical parameters including absorption coefficient, refractive index, extinction coefficient, real dielectric constant and imaginary dielectric constant in wavelength λ 800 nm are tabulated in Table 3.

The optical conductivity parameter (σ_{opt}) is a determination of the frequency response of the compound thin layer material when presented to electromagnetic light; "σ_{opt}" is allied to the refractive index (n) and optical absorption coefficient (α) by Eq. (11) [50].
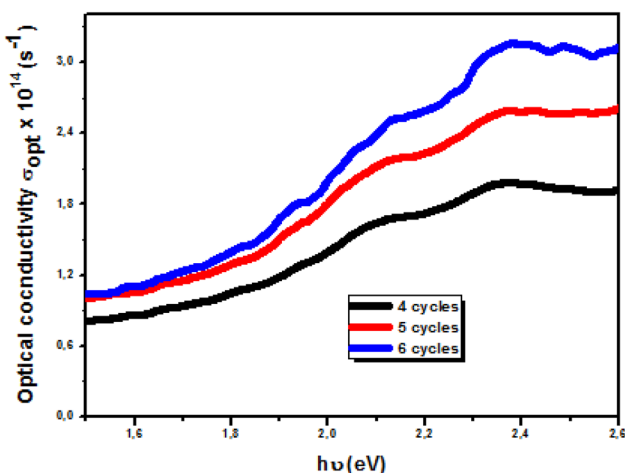
$$\sigma_{opt} = \frac{cn\alpha}{4\pi} \tag{12}$$

Figure 13 indicates the values of optical conductivity versus photon energy hν. We can see from Fig. 13 that "σ_{opt}" increases with dip-coating cycle increased in the energy range from 1.5 to 2.6 eV; this behavior is attributed to the behaviors of refractive index and absorption coefficient; also "σ_{opt}" increases with photon energy increased; the increase in photon energy advances the number of photo-excited electrons and their movement in thin film. This phenomenon helps the improvement of optical conductivity values. The values of optical conductivity are ranged from 0.80 to 3.16 $\times$ 10^{14} (s^{-1}). The great values of "σ_{opt}" are due to lesser transmittance and great values of refractive index and absorption coefficient.

3.4 Electrical properties

The control of electrical characteristics is significant to investigate the appropriateness of compound semiconductor thin films materials in solar cells applications. Four-point probe method was employed at room temperature for the study of sheet resistance (ρ_{sheet}), resistivity (ρ_s) and conductivity (σ_s). Generally, the film with great electrical conductivity is more adaptable for photovoltaic energy. The values of "ρ_s" were calculated from the determined "ρ_{sheet}" and film thickness "e" using Eq. (13) and "σ_s" were calculated from the inverse of "ρ_{sheet}."

$$\rho_s = \rho_{sheet} \times e \tag{13}$$

We can indicate from Table 4 the sheet resistance values decreased with dip-coating cycle increased. This behavior is due to more density and homogeneity of CNTS sample dip-coater at six cycles. The values of resistivity and sheet resistance are comparable to the other research groups [51, 52]. The values of electrical conductivity of the films deposited using four and five cycles are lower, and the electrical conductivity of the CNTS thin film deposited at six cycles is more adaptable for solar cell applications; probably the existence of secondary-phase NiS improves the electrical characteristics of CNTS thin films.

Fig. 13 Optical conductivity versus photon energy hν of dip-coated CNTS thin films

Table 4 Electrical characteristics of CNTS thin films

Dip-coating cycle	Sheet resistance ρ_{sheet} (kΩ/sq)	Resistivity ρ_s (Ω cm)	Conductivity (σ_s)(Ω cm)$^{-1}$
4	31.84	5.09	0.19
5	7.86	1.30	0.76
6	1.44	0.24	4.16

4 Conclusion

In brief, this paper proves the synthesis possibility of Cu_2NiSnS_4 thin films using sol–gel dip-coating method on ordinary glass substrates and annealed without sulfurization process. The effect of dip-coating cycle and annealing temperature was studied. All CNTS films indicated the formation of cubic structure with a privileged orientation along (111) plane. The crystallites size of all CNTS samples is in range between 6 and 9 nm. Raman experiments have confirmed the existence of cubic CNTS by strong peak at 332 cm^{-1}. The EDS analysis of the sample dip-coated at five cycles demonstrated near-stoichiometric CNTS thin film. SEM images present the homogenous films, the density of CNTS thin films increased with dip-coating cycle increased, and the estimated band gap is in the range of 1.5–1.64 eV. Some optical parameters of CNTS thin films such as refractive index, extinction coefficient, real and imaginary dielectric constants and optical conductivity are calculated from transmittance and absorbance spectra to enhance photovoltaic devices. The values of electrical sheet resistance obtained in the range of 1.44–31.84 (kΩ/sq). The studied physical properties demonstrated that CNTS thin films are suitable for photovoltaic application devices.

References

1. S. Binetti, A.L. Donne, V. Trifiletti, Front. Chem. **7**, 297 (2019)

2. M.A. Green, E.D. Dunlop, J. Hohl-Ebinger, M. Yoshita, N. Kopidakis, A.W.Y. Ho-Baillie, Prog. Photovolt. Res. **28**, 3–15 (2020)

3. K. Ito, T. Nakazawa, Jpn. J. Appl. Phys. **27**(11), 2094–2097 (1988)

4. A.V. Moholkar, S.S. Shinde, A.R. Babar, K.U. Sim, Y.B. Kwon, K.Y. Rajpure, P.S. Patil, C.H. Bhosale, J.H. Kim, Sol. Energy **85**(7), 1354–1363 (2011)

5. C. Yan, J. Huang, K. Sun, S. Johnston, Y. Zhang, H. Sun, A. Pu, M. He, F. Liu, K. Eder, L. Yang, J.M. Cairney, N.J.E. Daukes, Z. Hameiri, J.A. Stride, S. Chen, M.A. Green, X. Hao, Nat. Energy **10**, 2959 (2019)

6. W. Wang, M.T. Winkler, O. Gunawan, T. Gokmen, T.K. Todorov, Y. Zhu, D.B. Mitzi, Adv. Energy Mater. **4**(7), 6832–6840 (2014)

7. X. Liu, Y. Feng, H. Cui, F. Liu, X. Hao, G. Conibeer, D.B. Mitzi, M. Green, Prog. Photovolt. Res. **24**, 879–8982016 (2016)

8. D. Mora-Herrera, R. Silva-González, F.E. Cancino-Gordillo, Mou Pal **199**, 246–255 (2020)

9. L. Chen, H. Deng, J. Tao, H. Cao, L. Huang, L. Sun, P. Yanga, J. Chua, RSC Adv. **5**, 84295–84302 (2015)

10. G. Yang, X. Zhai, Y. Li, B. Yao, Z. Ding, R. Deng, H. Zhao, L. Zhang, Z. Zhang, Mater. Lett. **242**, 58–61 (2019)

11. A.M. Alanazi, F. Alam, A. Salhi, M. Missous, A.G. Thomas, P. Obrien, D.J. Lewis, RSC Adv. **9**, 24146–24153 (2019)

12. T. Wang, Q. Zhan, W. Cheng, J. Mater. Sci. **30**(3), 2285–2291 (2019)

13. H. Guo, C. Ma, Z. Chen, X. Jia, Q. Cang, N. Yuan, J. Ding, Sol. Energy **181**, 301–307 (2017)

14. H.I. Elsaeedy, J. Mater. Sci. **30**, 12545–12554 (2019)

15. A. Jariwala, T.K. Chaudhuri, S. Patel, A. Toshniwal, V. Kheraj, A. Ray, Mater. Lett. **215**, 118–120 (2018)

16. K. Mokurala, S. Mallick, P. Bhargava, S. Siol, T.R. Klein, M.F.A.M. van Hest, J. Alloy Compd. **725**, 510–518 (2017)

17. L. Shi, Y. Li, R. Zheng, ChemPlusChem **80**, 1533–1536 (2015)

18. S. Lu, H. Yang, F. Li, Y. Wang, S. Chen, G. Yang, Y. Liu, X. Zhang, Sci. Rep. **8**, 8714 (2018)

19. S. Dridi, N. Bitri, M. Abaab, Mater. Lett. **204**, 61–64 (2017)

20. C.L. Yang, Y.H. Chen, M. Lin, S.L. Wu, L. Li, W.C. Liu, X.S. Wu, F.M. Zhang, Mater. Lett. **166**, 101–104 (2016)

21. T.-X. Wang, Y.-G. Li, H.-R. Liu, H. Li, S.-X. Chen, Mater. Lett. **124**, 148–150 (2014)

22. S. Sarkar, B. Das, P.R. Midya, G.C. Das, K.K. Chattopadhyay, Mater. Lett. **152**, 155–158 (2015)

23. A. Kamble, K. Mokurala, A. Gupta, S. Mallick, P. Bhargava, Mater. Lett. **137**, 440–443 (2014)

24. D. Ait Elhaj, A. El-Kissani, M. Elyaagoubi, H. Ait Dads, F. Welatta, L. Nkhaili, H. Chaib, A. Outzourhit, Mater. Sci. Semicond. Process. **107**, 104811 (2020)

25. K. Mokurala, S. Mallick, P. Bhargava, S. Siola, T.R. Kleina, M.F.A.M. van Hesta, J. Alloys Compds. **725**, 510–518 (2017)

26. M. Faustini, B. Louis, P.A. Albouy, M. Kuemmel, D. Grosso, J. Phys. Chem. C **114**, 7637–7645 (2010)

27. T. Touam, M. Atoui, I. Hadjoub, A. Chelouche, B. Boudine, A. Fischer, A. Boudrioua, A. Doghmane, Eur. Phys. J. Appl. Phys. **67**, 30302 (2014)

28. H.-J. Chen, S.-W. Fu, T.-C. Tsai, C.-F. Shih, Mater. Lett. **166**, 215–218 (2016)

29. A. Ghosh, D.K. Chaudhary, A. Biswas, R. Thangavel, G. Udayabhanu, RSC Adv. **6**, 115204–115212 (2016)

30. S. Rondiya, N. Wadnerkar, Y. Jadhav, S. Jadkar, S. Haram, M. Kabir, Chem. Mater. **29**, 3133–3142 (2017)

31. D. Naveena, L. Thirumalaisamy, R. Dhanabal, K. Sethuraman, A.C. Bose, ACS Appl. Energy Mater. **3**(11), 10550–10559 (2020)

32. A. Chihi, M.F. Boujmil, B. Bessais, J. Mater. Sci. **30**(4), 3338–3348 (2019)

33. Y. Huang, E. Sutter, J.T. Sadowski, M. Cotlet, O.L.A. Monti, D.A. Racke, M.R. Neupane, D. Wickramaratne, R.K. Lake, B.A. Parkinson, P. Sutter, ACS Nano **8**(10), 10743–10755 (2014)

34. T. Chandel, V. Thakur, S. Halaszova, M. Prochazka, D. Hasko, D. Velic, R. Poolla, J. Electron. Mater. **47**(9), 5477–5487 (2018)

35. M.S. Niasari, F. Davar, H. Emadi, Chalcogenide Lett. **7**(12), 647–655 (2010)

36. E.A. Ramírez, A. Ramírez, G. Gordillo, Mater. Sci. Semicond. Process. **67**, 110–117 (2017)

37. P.R. Ghediya, T.K. Chaudhuri, Mater. Res. Express **5**, 085509 (2018)

38. A. Ziti, B. Hartiti, H. Labrim, S. Fadili, A. Ridah, M. Tahri, P. Thevenin, Appl. Phys. A **125**, 218 (2019)

39. H.I.H.A. El SaeedyEl Yakout, M.T. El Sayed, Appl. Phys. A **126**, 281 (2020)

40. P.S. Maldara, M.A. Gaikwada, A.A. Manea, S.S. Nikama, S.P. Desaia, S.D. Girib, A. Sarkarb, A.V. Moholkara, Sol. Energy **158**, 89–99 (2017)

41. N. Khemiri, S. Chamekha, M. Kanzaria **207**, 496–502 (2020)

42. N.A. Bakr, S.A. Salman, S.A. Hameed, Int. J. Appl. Eng. Res. **13**, 3379–3388 (2018)

43. M.A. Abed, N.A. Bakr, J. Al-Zanganawee, Chalcogenide Lett. **17**(4), 179–186 (2020)

44. T. Zdanowicz, T. Rodziewicz, M. Zabkowska-Waclawek, Sol. Energy Mater. Sol. Cells **87**, 757–769 (2005)

45. R.J. Deokate, R.S. Kate, S.C. Bulakhe, J. Mater. Sci. **30**(4), 3530–3538 (2019)

46. S. Islam, M.A. Hossain, H. Kabir, M. Rahaman, M.S. Bashar, M.A. Gafur, A. Kabir, M.M.R. Bhuiyan, F. Ahmed, N. Khatun, Int. J. Thin. Film Sci. Technol. **4**(3), 155–161 (2015)

47. A. Kotbi, B. Hartiti, S. Fadili, A. Ridah, P. Thevenin, Appl. Phys. A **123**, 379 (2017)

48. A.S. Hassanien, I.M. El-Radaf, Phys. B **585**(15), 412110 (2020)

49. A. Ziti, B. Hartiti, H. Labrim, S. Fadili, A. Batan, M. Tahri, A. Ridah, O. Mounkachi, A. Benyoussef, P. Thevenin, J. Mater. Sci. **30**, 13134–13143 (2019)

50. K. Sharma, A.S. Al-Kabbi, G.S.S. Saini, S.K. Tripathi, Mater. Res. Bull. **47**, 1400–1406 (2012)

51. S. Dridi, E. Aubry, N. Bitri, F. Chaabouni, P. Briois, Coatings **10**, 963 (2020)

52. X. Yu, A. Ren, F. Wang, C. Wang, J. Zhang, W. Wang, L. Wu, W. Li, G. Zeng, L. Feng, Int. J. Photoenergy **2014**, 1–6 (2014)